

# The mass and radius of 5 low-mass eclipsing binaries discovered with the WASP survey

S. Gill<sup>1</sup>, P. F. L. Maxted<sup>1</sup>, J. Southworth<sup>1</sup>, J. Kirkby-Kent<sup>1</sup>, D. F. Evans<sup>1</sup>, B. Smalley<sup>1</sup>, B. L. Gary<sup>2</sup>, U. G. Jørgensen<sup>2</sup>, M. Dominik<sup>3</sup>, C. Snodgrass<sup>4</sup>, and P. Longa<sup>5</sup>

<sup>1</sup> Astrophysics Group, Keele University, Staffordshire, UK

<sup>2</sup> Niels Bohr Institute & Centre for Star and Planet Formation, University of Copenhagen Øster Voldgade 5, 1350 - Copenhagen, Denmark

<sup>3</sup> SUPA, School of Physics & Astronomy, University of St Andrews, North Haugh, St Andrews KY16 9SS, UK

<sup>4</sup> School of Physical Sciences, Faculty of Science, Technology, Engineering and Mathematics, The Open University, Walton Hall, Milton Keynes, MK7 6AA, UK

<sup>5</sup> Unidad de Astronomía, Fac. de Ciencias Básicas, Universidad de Antofagasta, Avda. U. de Antofagasta 02800, Antofagasta, Chile

Received September 15, 2016; accepted March 16, 2016

## ABSTRACT

**Context.** There are few empirical mass and radius measurements for low-mass stars below  $0.4 M_{\odot}$ . Without such measurements we are unable to verify and test stellar models for stars at the bottom-end of the main-sequence which are notorious for being unreliable. M-dwarfs are the commonest stars in the Galaxy and contradictions between observations and evolutionary models needs addressing with more empirical calibrations of M-dwarfs.

**Aims.** We have measured the mass and radius of 5 low-mass eclipsing binary systems discovered by the WASP survey. We also assess the impact of third light contamination, choice of limb-darkening law, He-enhancement and mixing length parameter on measurements of mass and radius.

**Methods.** We use SuperWASP photometry to refine measurements of ephemerids and obtain first estimates of transit parameters. We simultaneously fit radial velocity measurements with follow-up photometry to find the best fitting orbital solution. We combine this solution with measurements atmospheric parameters to interpolate evolutionary models and estimate the mass of the primary star, and the mass of the M-dwarf companion. We assess how the best fitting orbital solution changes using two different limb-darkening laws and fitting assuming a third light contribution of 10 %. We also assess how the best fitting evolutionary model changes using different  $\alpha_{mlt}$  and He-enhancement.

**Results.** We report the mass and radius of 5 M-dwarfs which do not appear inflated with respect to evolutionary models. The primary star in two systems has evolved off the main-sequence into the post-main sequence blue hook resulting in two solutions for mass and age. We find that choices in He enhancement and  $\alpha_{mlt}$  can introduce a 2-4 % uncertainty in mass measurements. Third light and choice of limb-darkening law can introduce a 4-5 % and 4 % increase in radii respectively.

**Key words.** Stars: atmospheres, composition, binary

## 1. Introduction

Low-mass stars ( $\leq 0.6 M_{\odot}$ ) are challenging to study because of the low probability of finding eclipsing systems and their intrinsically low brightness. Careful observations of double-lined eclipsing binaries (SB2s) can result in (almost) model-independent estimates of mass and radius to a precision exceeding 1% in some cases (Griffin et al. 1997). Interferometry can be used to achieve similar results of nearby, single low-mass stars. Together, this synergy has yielded only 19 mass and radius measurements (Nefs et al. 2013; Zhou et al. 2014; von Boetticher et al. 2017) which reveal an unusual feature; some low-mass stars are hotter and larger than evolutionary models predict.

The stellar physics of low-mass stars is an interesting problem in its own right. M-dwarfs near the hydrogen burning limit ( $\sim 0.35 M_{\odot}$ ) are cool enough that their interiors approach the electron Fermi temperature, resulting in an electron degenerate gas where the classical Maxwellian description does not apply (Baraffe et al. 2003). A further complication arises from enhanced magnetic fields which may affect the evolution of M-dwarfs (Chabrier et al. 2007). Large magnetic fields are thought

to be induced by tidal interaction in close binaries, enhancing core rotation and the dynamo mechanism. This results in inhibited convection which may be responsible for inflating some stellar radii above those predicted by evolutionary models. However, studies of M-dwarfs in non-interacting systems (with interferometry) and those in binary systems are comparably inflated by around 3% (Spada et al. 2013) making it unclear whether tidal interactions can be blamed.

Using spectroscopy to measure the atmospheric composition of a low-mass star is challenging. Low surface temperatures permit molecules (TiO, VO, CaH, H<sub>2</sub>O, ...) to exist which manifest in a series of broad, and mostly blended lines in the optical. This problem is eased slightly in the infrared, where there are some non-blended regions allowing for equivalent-width measurements of the Na 1, Ca 1 and H<sub>2</sub>O-K2 index in the K band (Rojas-Ayala et al. 2012). The most common technique for determining the temperature of M dwarfs is comparing spectra to model atmospheres (Gaidos et al. 2014). The infrared flux method has also been extended from FGK stars to M dwarfs (Casagrande et al. 2008), however significant statistical devia-

tions from interferometric temperatures have been noted (Mann et al. 2015).

Large exoplanet surveys, such as the Wide Angle Search for Planets (WASP; Pollacco et al. 2006) search for  $0.8\text{--}2 R_{\text{Jup}}$  sized objects transiting solar-like stars. Objects in this range can have masses which span 3 orders of magnitude, from Saturn-like planets to M-dwarfs. Consequently, SuperWASP photometry has identified hundreds of FGK stars with transiting M dwarfs as a by-product of its successful exoplanet search<sup>1</sup>. These systems are important for several areas of Galactic, stellar and exoplanet studies and so we have invested hundreds of hours of telescope time to measure their spectroscopic orbits (Triaud et al. 2017).

The EBLM project (Triaud et al. 2013a; Gómez Maqueo Chew et al. 2014; Triaud et al. 2017; von Boetticher et al. 2017) is a series of papers aimed at measuring the mass and radius of M-dwarfs in hope of refining our understanding of low-mass stars. Four systems (WASP-30, J1219-39, J0113+31 and J0555-57) have been measured so far in this project, of which 1 star, WASP-30b, appears inflated while a second, J0113+31, appears  $\sim 1000\text{ K}$  hotter than expected through the analysis of secondary eclipses in infrared. A similar result is also seen for KIC 1571511 (Ofir et al. 2012). While Gómez Maqueo Chew et al. (2014) considers a variety of reasons for an enhanced surface temperature (of which they find none that are satisfactory), a solution may lay with tidal dissipation of eccentric systems. Such effects have implications for our understanding of the formation of hot Jupiters (Triaud et al. 2010) and determines the lifetime of extreme planetary systems (Levrard et al. 2009; Matsumura et al. 2010).

It is clear that we do not robustly understand stars at the bottom of the main sequence, and by extension the planets orbiting them. With publicity surrounding low mass stars increasing (e.g. TRAPPIST-1 and Proxima Centauri), we should invest time into what makes some stars anomalous so that we can make the most of the myriad of systems which will be discovered by space-based missions such as TESS (Ricker et al. 2014) or CHEOPS (Fortier et al. 2014). In this paper, we present high quality lightcurves and spectroscopic orbits of five EBLM systems allowing us to measure the mass and radius to the precision of a few percent in some cases. In section 2 we describe where we obtained and how we reduced our data, in section 3 describe how we extracted system parameters and we present and discuss our results in sections 4 & 6 respectively.

## 2. Observations and data reduction

In this section, we describe the data used to measure the physical properties of 5 EBLM systems. All five EBLMs were discovered using SuperWASP photometry (sec 2.1), but the quality of these light-curves are not good enough to measure mass and radius of both components to the desired precision of a few percent. We obtained follow-up photometry of better quality to provided better size estimates of both EBLM components.

We obtained spectroscopic orbits for each system. The evolution of the measured Doppler shift in a series of spectra across the orbit provides a mass constraint for both components in the system, as only the spectrum from the largest (solar-like) star is visible (SB1). We break the mass degeneracy by co-adding spectra to create a high SNR (signal-to-noise per Ångstrom) spectrum to estimate atmospheric parameters and interpolate evolutionary models for  $M_{\star}$ .

### 2.1. Photometry-optical: SuperWASP

The WASP survey (Pollacco et al. 2006) consists of two observatories at the South African Astronomical Observatory (SAAO), South Africa and the Observatory del Roque de los Muchachos, La Palma. Each site consists of an equatorial fork mount with eight 200 mm lenses covering approximately 64 square degrees. Data was reduced using a dedicated pipeline which removed systematic trends. In July, 2012 WASP-south changed optics to 85 mm, f/1.2 lenses in search of brighter exoplanet hosts (Smith & WASP Consortium 2014); we do not make use of the 85 mm data in this work.

Photometry from the SuperWASP cameras can suffer from a large amount of scatter (clouds and other non-optimal observing conditions). We cleaned the data by removing points which were not detrended in the standard WASP reduction pipeline and removed outliers which are above 0.5 mag from the median magnitude for each star. We exclude nights with less than 10 measurements and bin the phased light-curve into 500 bins. A measurement  $3\sigma$  or more from the mean in each bin is excluded, and an entire night excluded if more than a quarter of the nights data is excluded this way. The remaining light curves are then inspected by-eye to further exclude bad data points if necessary.

### 2.2. Photometry-optical: SAAO 1 m

The SAAO hosts a equatorial-mounted 1-m telescope built by Grub & Parsons and is equipped with a STE4 (1 K  $\times$  1 K) CCD camera. We operated this camera in  $2 \times 2$  binning mode to reduce readout time. We obtained a single transit light-curve for J2349-32, J2308-46 and J1436-13 in *I*, *R* and *R* filters respectively. Photometry was extracted using standard aperture photometry routines (Southworth et al. 2009) and uncertainties were estimated from photon counting statistics. A by-eye approach was used to clean the light-curve and select the best comparison star in the relatively narrow  $5'' \times 5''$  field. We observed a slow variation in differential magnitude with time corresponding to changes in the effective airmass. To correct this, we defined out-of-transit regions and used the IDL/AMOEBA<sup>2</sup> routine to fit a polynomial which minimises the square of the magnitude values resulting in light-curves which were normalised to zero differential magnitude.

### 2.3. Photometry-optical: HAO

We obtained optical photometry for J1847+37 from the Hereford Arizona Observatory (HAO). The HAO consists of two telescopes in separate observatories: HAO1 which houses a Celestron 11-inch CPC-1100 telescope and HAO2 which houses a Meade 14-inch LX200GPS. Single transits for J1847+37 were obtained in three different filters (CBB, *z'*, and *g'*) over different nights from HAO1. Aperture photometry was extracted using standard photometry routines with systematic trends removed and outliers rejected. We use transmission information of the telescope throughput, atmosphere, filter and CCD<sup>3</sup> to calculate the final transmission of HAO1 with the CBB filter (see Fig. 1). We decided to use the 4-parameter limb-darkening look-up table for the Kepler passband in substitution of the CBB filter due to the similarity in final transmission (A 4-parameter look-up table for the CBB filter does not exist). In Sect. (?) we fit the light-curve using quadratic limb-darkening over the Claret

<sup>2</sup> <http://www.harrisgeospatial.com/docs/AMOEBA.html>

<sup>3</sup> <http://www.brucegary.net/HAO/>

<sup>1</sup> These systems are named EBLMs (eclipsing binary low-mass).

law. We use the final response function in Fig. 1 along with estimates of atmospheric parameters (from spectroscopy and photometry) to calculate quadratic coefficients using *LDTK* (Parviainen & Aigrain 2015).

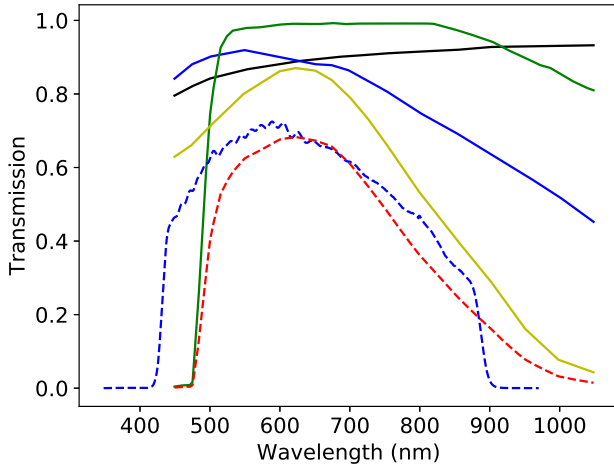


**Fig. 1.** The transmission properties of HAO-11. We plot the atmospheric transmission (black), the transmission of the HAO1 telescope (blue-solid), the CBB filter (green) and CCD response. We plot the final response of HAO-1 with the CBB filter (red-dashed) along with the Kepler transmission (blue-dashed).

## 2.4. Photometry-optical: CTIO

The Cerro Tololo Inter-American Observatory (CTIO) is located 80 km to the East of La Serena, Chile, at an altitude of 2200 meters. The principle telescopes on site are the 4-m Victor M. Blanco Telescope and the 4.1-m Southern Astrophysical Research (SOAR) telescope, and one of the two telescopes making the Gemini observatory. Amongst these is the 0.9 m SMARTS telescope, which was used with the TEK2K camera to observe a single transit simultaneously in bands  $g'$ ,  $r'$ ,  $i'$ , and  $z'$  for J0218-31 on the 14th November, 2010. Photometry was extracted via standard routines with systematic trends and outliers removed.

## 2.5. Spectroscopy: CORALIE

CORALIE is a fiber-fed échelle spectrograph installed on the 1.2-m Leonard Euler telescope at the ESO La Silla Observatory and has a resolution-per-Ångström (R) between 50,000 and 60,000 (Queloz et al. 2001; Wilson et al. 2008). We obtained 20 observations for J2349-32, 19 for J2308-46 and 70 for J0218-31 which include the Rossiter-McLaughlin effect. The spectra for each star was processed with the CORALIE standard reduction pipeline (Baranne et al. 1996). Radial velocity measurements were obtained via standard cross-correlation techniques and checked for suspect bisector spans and obvious outliers. Each spectrum was corrected into a laboratory reference frame and co-added onto a common wavelength range. Maximum and median filters were applied to identify continuum regions which were fitted with spline functions (1 every nm) to normalise the spectra (provided within *ISPEC*; Blanco-Cuadras et al. 2017).

## 2.6. Spectroscopy: INT

We obtained spectra for the only northern target, J1847+39, using the intermediate dispersion spectrograph (IDS) mounted on the 2.54 m Isaac Newton telescope (INT) at the Roque de Los Muchachos Observatory. We used the *H1800VP* grating to capture a small region around the  $H\alpha$  line with  $R \approx 10,000^4$ . Radial velocity measurements were obtained via standard cross-correlation techniques and checked for suspect bisector spans and obvious outliers. Each spectrum was corrected into a laboratory reference frame and co-added onto a common wavelength range. The relatively small wavelength range does not permit the use of maximum and median filters to normalise the spectra. We instead choose suitable continuum regions and fit a second-order polynomial.

## 2.7. Lucky imaging

We obtained high-resolution images with the lucky imaging technique of J2308-46 and J2349-32 on the nights of 07-08 July 2017, in order to search for stars contributing contaminating light, as well as potential bound companions to the eclipsing binaries. The observations were conducted using the Two Colour Instrument (TCI) on the Danish 1.54m Telescope at La Silla Observatory. The TCI consists of two Electron Multiplying CCDs capable of imaging simultaneously in two passbands at a frame rate of 10Hz, with a field of view of  $40 \times 40$  arc-seconds square. The ‘red’ arm has a passband similar to a combined  $i + z$  filter or the Cousins  $I$  filter, whilst the ‘visible’ arm has a mean wavelength close to that of the Johnson  $V$  filter. A detailed description of the instrument and lucky imaging reduction pipeline can be found in Skottfelt et al. (2015) and Harpsøe et al. (2012) respectively.

The observations and data reduction were carried out using the method outlined in Evans et al. (2016), which is briefly described here. Both targets were observed for 170s. The raw data were reduced automatically by the instrument pipeline, which performs bias and flat frame corrections, removal of cosmic rays, and determination of the quality of each frame, with the end product being ten sets of stacked frames, ordered by quality. The data were run through a custom star detection algorithm described in Evans et al. (2016), which is designed to detect close companion stars that may not be fully resolved.

## 3. Data characterisation

In this section we describe the process of measuring the physical properties of each EBLM system. Transit photometry provides size constraints on the system and radial velocity measurements provide relative constraints on the mass of each star. In this section, we describe how we fit spectroscopy, radial velocities and light-curves to obtain the best-fitting orbital solution. We combine this solution with atmospheric parameters to interpolate evolutionary models and break the mass degeneracy which accompanies SB1s.

### 3.1. Photometry

We have used empirical colour – effective temperature and colour – surface brightness relations to estimate the effective temperatures of the systems we have studied. We extracted photometry for each target from the following catalogues –  $B_T$  and

<sup>4</sup> Calculated from <http://www.ing.iac.es/astronomy/instruments/ids/idsgrat>,

$V_T$  magnitudes from the Tycho-2 catalogue (Høg et al. 2000);  $B$ ,  $V$ ,  $g'$ ,  $r'$  and  $i'$  magnitudes from data release 9 of the AAVSO Photometric All Sky Survey (APASS9, Henden et al. 2016);  $J$ ,  $H$  and  $K_s$  magnitudes from the Two-micron All Sky Survey (2MASS, Skrutskie et al. 2006);  $i'$ ,  $J$  and  $K$  magnitudes from the Deep Near-infrared Southern Sky Survey (DENIS, Epchtein et al. 1997). Not all stars have data in all these catalogues and is summarised in Table 1.

Our model for the observed photometry has the following parameters –  $g'_0$ , the apparent  $g'$ -band magnitudes corrected for extinction;  $T_{\text{eff}}$  the effective temperature;  $E(B - V)$ , the reddening to the system;  $\sigma_{\text{ext}}$  the additional systematic error added in quadrature to each measurement to account for systematic errors. For each trial combination of these parameters we use the empirical colour – effective temperature relations by Boyajian et al. (2013) to predict the apparent magnitudes for each star in each of the observed bands. We used the same transformation between the Johnson and 2MASS photometric systems as Boyajian et al. 2013. We used Cousins  $I_C$  as an approximation to the DENIS Gunn  $i'$  band and the 2MASS  $K_s$  as an approximation to the DENIS  $K$  band (see Fig. 4 of Bessell 2005). We used interpolation in Table 3 of Bessell (2000) to transform the Johnson  $B$ ,  $V$  magnitudes to Tycho-2  $B_T$  and  $V_T$  magnitudes. We assume that the extinction in the  $V$  band is  $3.1 \times E(B - V)$ . Extinction in the SDSS and 2MASS bands is calculated using  $A_r = 2.770 \times E(B - V)$  from Fiorucci & Munari (2003) and extinction coefficients relative to the  $r'$  band from Davenport et al. (2014).

We used EMCEE (Foreman-Mackey et al. 2013) to sample the posterior probability distribution for our model parameters. We used the reddening maps by Schlafly & Finkbeiner (2011) to estimate the total line-of-sight extinction to each target,  $E(B - V)_{\text{map}}$ . This value is used to impose the following (unnormalized) prior on  $\Delta = E(B - V) - E(B - V)_{\text{map}}$ :

$$P(\Delta) = \begin{cases} 1 & \Delta \leq 0 \\ \exp(-0.5(\Delta/0.034)^2) & \Delta > 0 \end{cases}$$

The constant 0.034 is taken from Maxted et al. (2014) and is based on a comparison of  $E(B - V)_{\text{map}}$  to  $E(B - V)$  from Strömgren photometry for 150 A-type stars. We assume that the flux contribution from the M-dwarf companion is negligible compared to the solar-like star.

The empirical colour – temperature relations we have used are valid over the approximate range  $T_{\text{eff}} = 3450 \text{ K}$  to  $8600 \text{ K}$ . Our results may be biased in systems where one of the stars has an effective temperature near either of these limits because we exclude trial solutions with any  $T_{\text{eff}}$  value outside this range. Between these limits we use uniform priors on the values of  $T_{\text{eff}}$ . We also use uniform priors for  $g'_0$ . We draw 10,000 steps from 100 walkers as a burn-in. We then draw a further 10,000 steps and select the step with the lowest value of  $\Delta$ , with uncertainties equal to the standard deviation in the second chain. An example posterior probability distribution for J2308-46 is shown in Fig. 2.

### 3.2. Spectroscopic analysis

To be inserted once wavelet paper is accepted.

### 3.3. Ephemerides and first-order transit parameters

We use SuperWASP photometry to refine ephemerides and obtain first estimates for transiting parameters. Using the framework of Beatty et al. (2007), we obtain first order approximations

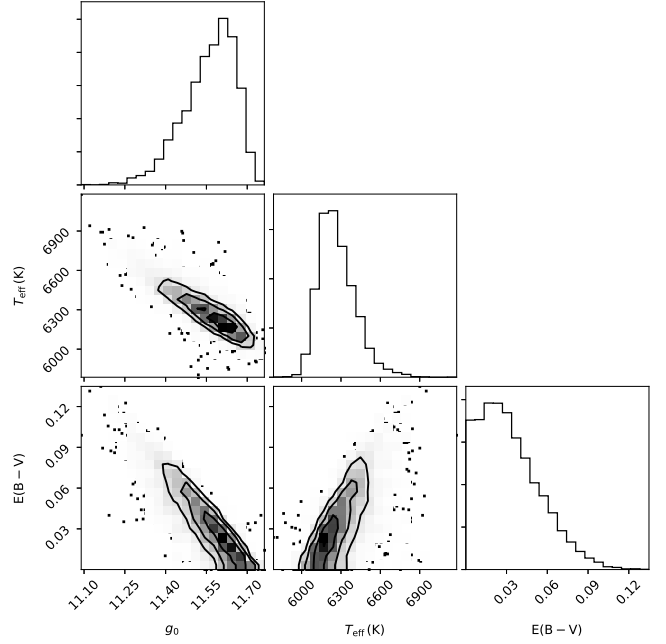


**Fig. 2.** The posterior probability distribution of EBLM J2349-32 from photometric fitting.

of the ratio of semi-major axis,  $a$ , and the radius of the primary star,  $R_\star$ ,

$$\frac{R_\star}{a} \approx \pi \frac{\Delta t_{tr}}{P}, \quad (1)$$

and the ratio of the radii,  $k$

$$k = \frac{R_2}{R_\star} \approx \sqrt{\Delta m}, \quad (2)$$

where  $\Delta t_{tr}$  is the transit width and  $\Delta m$  is the depth of transit. The SuperWASP photometry was fitted independently using models from ELLC (?). The free parameters explored were  $P$ ,  $dP/dt$ ,  $T_0$ ,  $k$ ,  $R_\star/a$  and the magnitude zero-point. A chi-squared minimization routine was used to find the best fitting solution, which was used as a starting point for fitting follow-up photometry in Section 3.4. To refine ephemerides we obtain  $P$  and  $T_0$  for each unique year of SuperWASP photometry and minimise the correlation between  $T_0$  and  $P$ . These values are quoted in Table. 1.

We use SuperWASP photometry to check for rotational modulation and ellipsoidal variation. We use the package PERIOD04 (Lenz & Breger 2005) to search for frequencies and remove the frequency until no appreciable signals remain (Fig. 3). We then phase-fold the SuperWASP light-curve to assess the origin of each frequency.

### 3.4. Orbital fit

With higher quality data, we can accurately estimate features that shape a transit light-curve: impact parameter ( $b$ ), limb-darkening effects, transit depth and width. We choose to simultaneously fit the radial velocity measurements along with the photometry to provide eccentricity and periastron constraints that ultimately govern size estimates of the transiting M-dwarf.

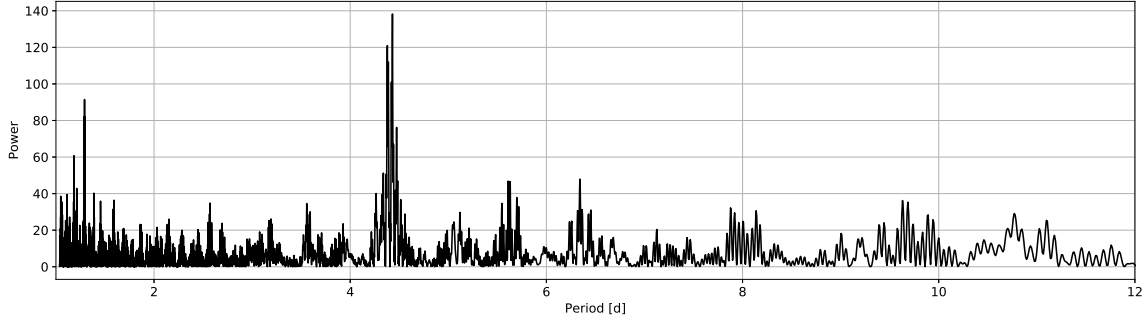


**Fig. 3.** The power spectrum of EBLM J2349-32 using 3 years of SuperWASP photometry.

We fit all follow-up photometry and radial velocity measurements together to solve for the orbital properties of each system. We performed a  $\chi^2$  fit in a Bayesian framework to estimate the posterior probability distribution (PPD) of each modeled parameter. The vector model of parameters includes photometric zero-points,  $zp$ ,  $R_*/a$ ,  $b$ ,  $T_0$ ,  $P$ ,  $K$ ,  $\gamma$  and  $d(\gamma)/dt$ . Instead of fitting  $\omega$  and  $e$ , we choose to use less correlated parameters  $f_c = \sqrt{e} \cos \omega$  and  $f_s = \sqrt{e} \sin \omega$ . We independently fitted the RV measurements and applied the Lucy significance test (Lucy 2013) to see if a circular or eccentric solution is preferred. Despite the outcome of this test, we still include  $f_c$  and  $f_s$  in the orbital fit to ensure all systems are fitted under the same framework. We also include a jitter term,  $J$ , to account for spot activity introducing noise in the radial velocity measurements. For J0218-31, we had Rossiter McLaughlin measurements. This required two more de-correlated parameters,  $\sqrt{V} \cos i \sin \lambda$  and  $\sqrt{V} \sin i \cos \lambda$ , where  $|\lambda|$  is the orbital obliquity. We fit a limb-darkening temperature,  $T_{ld}$ , which is used to interpolate coefficients for the Claret limb-darkening (provided with the python package `ELLIC` (Maxted 2016)) law using fixed values of  $[\text{Fe}/\text{H}]$  and  $\log g$  from spectroscopy. We use a Gaussian prior for  $T_{ld}$  with width equal to the uncertainty of  $T_{eff}$  measurements from the wavelet method, 86 K.

We generate radial velocity and photometric models using the python package `ELLIC`. We compare these models to data in a Bayesian framework; we use the likelihood function  $\mathcal{L}(\mathbf{d}|\mathbf{m}) = \exp(-\chi^2/2)$ , where

$$\chi^2 = \sum_{i=1}^{\infty} \frac{(m_i - m_{model})^2}{(\sigma_{m_i}^2)} + \sum_{i=1}^{\infty} \frac{(rv_i - rv_{model})^2}{(J\sigma_{rv_i}^2)} + \sum_{i=1}^{\infty} \frac{(T_{eff} - T_{ld})^2}{(\sigma_{T_{eff}}^2)}. \quad (3)$$

We initiated 50 walkers and generated 50,000 steps from each, after an initial burn-in phase of 50,000 steps. We initially selected the model with the highest value of  $\mathcal{L}(\mathbf{d}|\mathbf{m})$  with uncertainties equal to the standard deviation of each parameter in the second set of draws. However, we occasionally found these values to be up to  $2\sigma$  away from the median value and so we chose the median value instead.

### 3.5. Mass and age estimates

Obtaining the mass of both components and the age ( $\tau$ ) of the system is non-trivial. One approach by Hebb et al. (2009) is to use Kepler's equation to obtain first estimate of the primary star density,

$$\rho_* = \frac{3\pi}{GP^2} \left( \frac{a}{R_*} \right)^3 - \frac{3M_2}{4\pi R_*^3} \quad (4)$$

and combine it with measurements  $T_{eff}$  and  $[\text{Fe}/\text{H}]$  to interpolate stellar models for  $M_*$  and  $\tau$ . This is typically repeated with a better estimate of  $M_*$  until a solution is converged upon. Another approach makes use of empirical mass and radius calibrations (Southworth 2011; Torres 2013) to obtain  $M_*$  and  $R_*$ , which can be combined with  $k$  and eqn. 4 to obtain  $M_2$  and  $R_2$ . Another approach by Triaud et al. (2013b) is to mix the two methods while fitting alongside orbital parameters. The mass function (Hilditch 2001; Triaud et al. 2013b) can be expressed in terms of radial velocity parameters,

$$f(m) = \frac{(M_2 \sin i)^3}{(M_* + M_2)^2} = (1 - e^2)^{\frac{3}{2}} \frac{PK^3}{2\pi G}. \quad (5)$$

Both sides of Eqn. 5 are equated and numerically solved for  $M_2$  assuming an initial guess of  $M_*$  from empirical calibrations. Stellar models can then be interpolated to give a new estimate of  $M_*$  which can then be re-inserted into the begging of the next iteration. A final method relies three assumptions: (1) the circularisation timescale ( $\tau_{circ}$ ) is much shorter than  $\tau$ , (2) the rotation is synchronised ( $\tau \gg \tau_{syn}$ ) and (3) that rotational and orbital inclination are assumed to be the same. With theses assumptions it is possible to directly calculate the mass and radius of both components without dependency on stellar models (see Eqns. 14-17 of Beatty et al. 2007).

To estimate the mass and age of the primary star we combined the best fitting orbital solution (Sect. 3.4) and atmospheric parameters (Sect. 3.1 & 3.2) to interpolate evolutionary models computed with the `GARSTEC` stellar evolution code (Weiss & Schlattl 2008). We use a modified version of the open-source code `BAGEMASS` (?), tailored exclusively for EBLM systems (EBLMMASS). EBLMMASS uses the jump parameters of age, primary mass ( $M_*$ ), the initial iron abundance  $[\text{Fe}/\text{H}]_i$ ,  $M_2$  and the full-width half maximum of the transit. The vector model of parameters is given by  $\mathbf{m} = (f(m), T_{eff}, \log L_*, [\text{Fe}/\text{H}]_s, R_*/a)$  where  $\log L_*$  is the luminosity of the primary star and  $[\text{Fe}/\text{H}]_s$  is the surface metal abundance and differs from the initial abundance ( $[\text{Fe}/\text{H}]_i$ ) due to diffusion and mixing processes throughout stellar evolution. To obtain  $M_2$  from the  $f(m)$ ,  $M_*$  and  $P$  we need to know inclination from the transit light-curve. Degeneracies between  $i$ ,  $R_*/a$  and  $k$  are such that we choose to fit the full-width half maximum of the transit,

$$fwhm = \frac{R_*}{a} \frac{\sqrt{1 - b^2}}{\pi}. \quad (6)$$

instead of the  $i$ .

The GARSTEC evolutionary models are the exact same ones used in BASGEMASS. We implement a Gaussian prior on  $[\text{Fe}/\text{H}]_s$  from spectroscopy and use a uniform prior for age and  $M_\star$ . We ran a burn-in chain of 100,000 draws before drawing 50,000 values to match that of the orbital fit. We combined the PPDs for  $M_\star$  and  $M_2$  from EBLMMASS with the PPD for orbital period  $P$  from the orbital fit to calculate the PPD for  $R_\star$ ,  $R_2$  using the semi-major axis  $a$  (Hilditch 2001):

$$a = 4.20944009361 \times P^{\frac{2}{3}} (M_\star + M_2)^{\frac{1}{3}}. \quad (7)$$

We use an up-to-date constant from IAU resolution B3 (Mamajek et al. 2015). Similar to Sect. 3.4, we found the solution with highest value of  $\mathcal{L}(\mathbf{d}|\mathbf{m})$  could be up to  $2\sigma$  away from the median value and so we decide to use the median value with uncertainties equal to the standard deviation of the PPD for each parameter. An example of this problem is seen in Fig. 4.

## 4. Results

### 4.1. EBLM J2349-32

EBLM J2349-32 was observed over three unique years with WASP-south. Over these seasons we found signals of 4.421  $d$ , 4.345  $d$  and 4.421  $d$  with amplitudes of 0.6 %, 0.7 % and 0.4 % respectively. Each of these signals has a false-alarm probability  $< 0.00001$  and so we conclude a rotational period of  $4.396 \pm 0.025 d$ . We fit 10 photometry measurements with an estimate of reddening from NED to estimate  $T_{\text{eff}} = 6085 \pm 88 K$  (spectral type F8). The best fitting reddening  $E(B - V) = 0.017 \pm 0.017$  corresponds a distance  $X$  parsecs away. This system was included in the first data release of GAIA (Gaia Collaboration et al. 2016a);  $G$ -mag was measured to be 11.413 with parallax of 3.43 (11.18 ly). In total, 17 spectra were median combined with a signal-to-noise ratio per Ångström (SNR)  $\sim 40$  and suggests a relatively hotter, but metal deficient F7 star. We found evidence of a small lithium opacity at 670.7 nm which was fitted by synthesis to determine  $\log A_{\text{Li}} + 12 = 2.4 \pm 0.08$ . EBLM J2349-32 was observed with lucky imaging on 2017-07-08, with two companion stars being detected. A close companion was found at a separation of  $1.402 \pm 0.013$  arc-seconds and position angle of  $308.6 \pm 0.6$  deg (Fig. 5). We measured the companion to be  $5.55 \pm 0.08$ mag, fainter in the TCI red images; the companion was not sufficiently resolved in the TCI visible images to obtain any reliable measurements. A second, distant companion was detected at a separation of  $25.70 \pm 0.07$  arc-seconds, position angle of  $218.6 \pm 0.3$  deg. We find that it is  $9.0 \pm 0.3$ mag, fainter with the TCI red images and  $8.5 \pm 0.3$ mag, fainter in the visible images. This more distant companion is included in the Gaia DR1 catalogue with Source ID 2314099173307737088. If the closest companion is blended in the CORALIE and SAO 1-m apertures, we estimate it to contribute 0.6 % of the light - far below the sensitivity of the data.

A Lucy significance test to found that a circular orbit is preferred over an eccentric one. The RVs were then fitted simultaneously with a single transit in I-band from the SAO-1m telescope to obtain the best fitting orbital solution. The PPD for eccentricity is consistent with a circularised system ( $e \leq 0.05$  to  $5\sigma$ ). We find a negligible drift in systematic velocity of  $(4 \pm 12 \text{ ms}^{-1} \text{ yr}^{-1})$  which is inconsistent with a tertiary component.

We combine the best fitting orbital solution and atmospheric parameters in *eblmass* to estimate the masses, radii and age

of the system (Fig. 4). The host star appears to be solar-like in scale and mass but much hotter and metal deficient; the degeneracy between these two parameters is not enough to account for  $\Delta T_{\text{eff}} \approx 350 K$  ( $\Delta[\text{Fe}/\text{H}]$  of 0.1 dex equates to a change of approximately 80 K. The secondary component appears to be an M-dwarf below the fully convective limit ( $\approx 0.35 M_\odot$ ). The secondary is consistent with evolutionary models at solar metallicity and relatively inflated to those at  $[\text{Fe}/\text{H}] = -0.5$ .

### 4.2. EBLM J2308-46

EBLM J2308-46 has SuperWASP photometry spanning 5 years. We find moderately strong transit signals in only 2 seasons of data, and a strong  $P/2$  signal in 4 seasons of data. Phase folding SuperWASP photometry the at the  $P/2$  period reveals a moderate ellipsoidal variation with an amplitude of 5 mmag (Fig. 9) suggesting that stars are tidally interacting. **sentence about rotational modulation.** We fitted 10 photometry measurements with an estimate of reddening from NED to estimate  $T_{\text{eff}} = 6268 \pm 136 K$ . The best fitting  $E(B - V) = 0.032 \pm 0.022$  corresponds to a distance  $X$  parsecs away. This system is included in the GAIA DR1 catalogue with Source ID 6539811294185397120 ( $G$  mag = 11.361) but does not include a parallax measurement. J2308-46 was observed with lucky imaging on 2017-07-07, with only a single, faint companion being found, located  $21.38 \pm 0.04$  arc-seconds away at a position angle of  $208.2 \pm 0.4$  deg (Fig. 7). We measured magnitude differences of  $8.2 \pm 0.3$ mag, in the TCI red images and  $8.0 \pm 0.2$ mag, in the TCI visible images. This object is included in the Gaia DR1 catalogue with Source ID 6539811289890737408 (Gaia Collaboration et al. 2016b,a).

We fixed parameters associated with ellipsoidal variation to produce a good out-of-transit fit to the SuperWASP photometry ( $q = M_2/M_\star = 0.05$ , gravity darkening coefficient = 0.1) to estimate transit parameters and refine ephemerides;  $q$  and the gravity darkening coefficients were not fitted. We co-added 22 spectra to produce a spectrum with SNR of 20. Wavelet analysis determined the primary star to be a fast rotating ( $v \sin i \sim 39 \text{ km s}^{-1}$ ) F7 spectral type that is relatively metal poor ( $[\text{Fe}/\text{H}] = -0.15$ ). This star appears to be close to the Kraft break (Kraft 1967) which separates stars with deep convective envelopes and efficient dynamos to those without. Magnetic fields from these dynamos maintain a transfer of angular momentum to stellar wind resulting in magnetic braking. The high rotation rate opposed precise radial velocity measurements, and we excluded 5 RVs due to suspect bisector spans and obvious outliers. We independently fitted the RVs with both a circular and elliptical models, prior to fitting with photometry, and found that a elliptical model is favored with the Lucy significance test.

Fitting the follow-up photometry jointly with radial velocity measurements was non-trivial as clear systematics remained in the SAO 1-m light-curve after initial detrending. We initially fitted EBLM J2308-46 in the same framework as J2349-32 but found an unacceptable fit around contact point 2 (see top panel of Fig. 9). We attempted to further detrend the light-curve with airmass, CCD position and time but were unsuccessful. We decided generate a red noise model using Gaussian processes (GP). We used the CELERITE package (Foreman-Mackey et al. 2017) framework with a Matern 3/3 kernel along with a mean light-curve model from the best fitting solution without GP to produce a suitable red noise model (see top plot of Fig. 9). We attempted to fit  $\log \sigma_r$  and  $\log \rho$  but found both are highly volatile parameters which do not converge well. The parameter  $\log \rho$  describes the frequency of the kernel which tended to a over-fitted light-curve it remained as a free parameter in the joint fit. We tried fixing

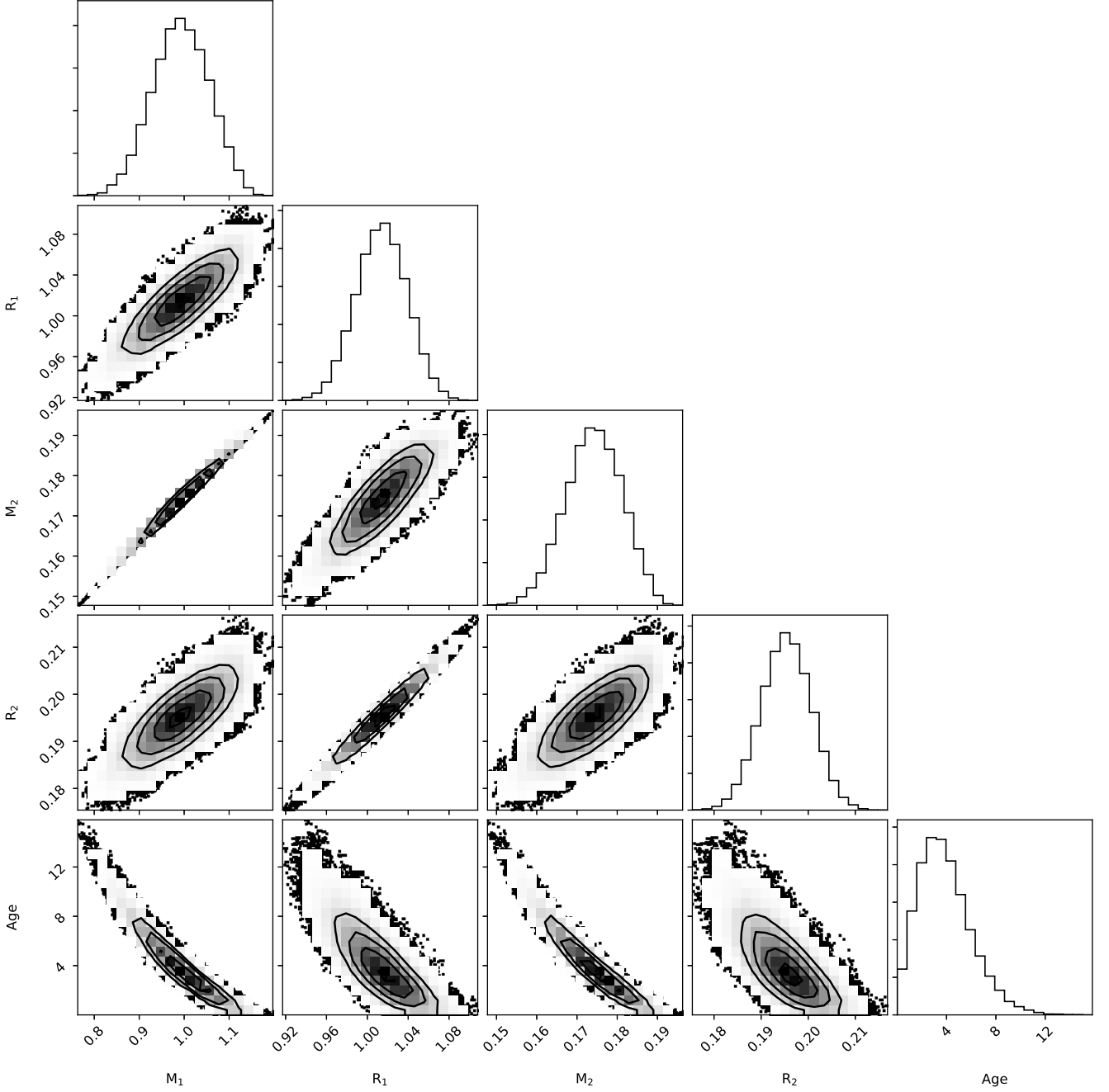


**Fig. 4.** The posterior probability distributions from EBLMMASS for EBLM J2349-32.

$\log_p$  and just fitting  $\log_\sigma$  but found poor convergence. Instead, we changed  $\log_p$  and  $\log_\sigma$  until an acceptable red-noise model was found ( $\log_\sigma = 2$ ,  $\log_p = 2$ ) and fixed these parameters during the fit.

The primary star is slightly evolved along the sub-giant branch and overlaps part of the Heney hook (post main-sequence blue hook). This occurs in massive stars ( $\geq 1.3M_\odot$ ) when the CNO cycle diminishes at the end of its main sequence life. During this phase, a star loses more energy at the surface than is produced at the core resulting in a loss of thermal equilibrium, and overall contraction. Once the core has contracted and heated up enough, the CNO cycle ignites again in a shell around the helium core marking the start of the hydrogen-shell burning

phase. The result is a *hook*-like evolutionary path on the classical Hertzsprung–Russell diagram making it difficult to discern which part of the hook J2308-46 is on (see Fig. 8). This results PPDs from EBLMMASS for  $M_\star$  and  $M_2$  to have two peaks instead of one, of which we fit a double Gaussian (100 bins). We find that the younger solution ( $3.98 \pm 0.86$  Gyr) is preferred over the older ( $5.81 \pm 1.0$  Gyr) with a Bayes factor ( $\mathcal{L}(3.98 \text{ Gyr})/\mathcal{L}(5.81 \text{ Gyr}) \sim 3.18$  (Fig. 8). We report both solutions in Table. 1 but use the younger, more massive solution for the rest of this paper.

**Table 1.** Overview of 5 EBLM systems.

	J2349-32	J2308-46	J0218-31	J1847+39	J1436-13
Spectral type	F5V	F5V	F5V	F5V	F5V
$\alpha$	23 <sup>h</sup> 49 <sup>m</sup> 15.23 <sup>s</sup>	23 <sup>h</sup> 08 <sup>m</sup> 45.66 <sup>s</sup>	02 <sup>h</sup> 18 <sup>m</sup> 13.24 <sup>s</sup>	18 <sup>h</sup> 47 <sup>m</sup> 52.34 <sup>s</sup>	14 <sup>h</sup> 36 <sup>m</sup> 46.42 <sup>s</sup>
$\delta$	-32 <sup>h</sup> 46 <sup>deg</sup> 17.5 <sup>arcmin</sup>	-46 <sup>deg</sup> 06 <sup>arcmin</sup> 36.6 <sup>arcmin</sup>	-31 <sup>deg</sup> 05 <sup>arcmin</sup> 17.3 <sup>arcmin</sup>	+39 <sup>deg</sup> 58 <sup>arcmin</sup> 51 <sup>arcmin</sup>	+13 <sup>deg</sup> 32 <sup>arcmin</sup> 35.5 <sup>arcmin</sup>
Vmag	11.53	11.36	9.96	11.73	
from photometry					
$T_{\text{eff,phot}}$ (K)	6085 $\pm$ 88	6268 $\pm$ 136	6014 $\pm$ 99	6205 $\pm$ 218	6078 $\pm$ 356
Distance (pc)	-	-	-	-	-
$E(B - V)$	0.017 $\pm$ 0.017	0.032 $\pm$ 0.022	0.030 $\pm$ 0.020	0.073 $\pm$ 0.042	0.031 $\pm$ 0.024
$g_0$	11.708 $\pm$ 0.067	11.565 $\pm$ 0.092	10.045 $\pm$ 0.082	11.753 $\pm$ 0.167	12.502 $\pm$ 0.121
from spectroscopy					
$T_{\text{eff}}$ (K)	6128 $\pm$ 124	6183 $\pm$ 124	6099 $\pm$ 124	6200 $\pm$ 124	6312 $\pm$ 124
$\log g$ (dex)	4.42 $\pm$ 0.21	4.21 $\pm$ 0.21	4.05 $\pm$ 0.21	4.44 $\pm$ 0.21	4.25 $\pm$ 0.21
$\xi_t$ (kms <sup>-1</sup> )	1.05 $\pm$ 1.50	1.07 $\pm$ 1.50	1.03 $\pm$ 1.5	1.08 $\pm$ 1.50	1.14 $\pm$ 1.50
$v_{\text{mac}}$ (kms <sup>-1</sup> )	4.23 $\pm$ 1.50	4.95 $\pm$ 1.50	4.94 $\pm$ 1.50	4.55 $\pm$ 1.50	5.41 $\pm$ 1.50
$V \sin i$ (kms <sup>-1</sup> )	11.50 $\pm$ 0.8	39.83 $\pm$ 0.8	9.00 $\pm$ 0.80	20.00 $\pm$ 0.80	20.00 $\pm$ 0.80
[Fe/H]	-0.28 $\pm$ 0.14	-0.15 $\pm$ 0.14	0.15 $\pm$ 0.12	-0.25 $\pm$ 0.20	-0.10 $\pm$ 0.12
$\log A(\text{Li})$	2.4 $\pm$ 0.1	-	3.1 $\pm$ 0.1	-	-
from orbital fit					
$R_*/a$	0.0928 $\pm$ 0.0003	0.1934 $\pm$ 0.0030	0.0982 $\pm$ 0.0029	0.0570 $\pm$ 0.0005	0.1070 $\pm$ 0.0005
$R_2/a$	0.0278 $\pm$ 0.0003	0.0239 $\pm$ 0.0001	0.0165 $\pm$ 0.0006	0.0162 $\pm$ 0.0002	0.0290 $\pm$ 0.0040
$k$	0.2996 $\pm$ 0.0002	0.1234 $\pm$ 0.0007	0.1685 $\pm$ 0.0033	0.2842 $\pm$ 0.0010	0.2721 $\pm$ 0.0403
$b$	0.01 $\pm$ 0.01	0.05 $\pm$ 0.08	0.72 $\pm$ 0.02	0.41 $\pm$ 0.02	0.86 $\pm$ 0.07
$T_{\text{eff,ld}}$ (K)	6105 $\pm$ 260	6530 $\pm$ 320	6109 $\pm$ 400	6860 $\pm$ 260	6072 $\pm$ 360
$K$ (kms <sup>-1</sup> )	21.97 $\pm$ 0.02	24.02 $\pm$ 0.18	27.80 $\pm$ 0.01	27.00 $\pm$ 0.83	46.50 $\pm$ 0.07
$f s$	0.026 $\pm$ 0.023	-0.0102 $\pm$ 0.050	-0.003	0.070 $\pm$ 0.052	0.022 $\pm$ 0.052
$f c$	-0.087 $\pm$ 0.009	0.110 $\pm$ 0.047	0.002	-0.451 $\pm$ 0.013	0.032 $\pm$ 0.027
$e$	0.008 $\pm$ 0.002	0.024 $\pm$ 0.015	0	0.209 $\pm$ 0.014	0.002 $\pm$ 0.002
$\omega$ (°)	163 $\pm$ 14	318 $\pm$ 18	-	351 $\pm$ 18	34 $\pm$ 24
$T_0$ (HJD)	2454215.89918 $\pm$ 0.00007	2458439.61175 $\pm$ 0.00010	2455613.39969 $\pm$ 0.00005	2454234.68973 $\pm$ 0.00010	2454625.48447 $\pm$ 0.00008
$P$ (d)	3.5496959 $\pm$ 0.0000033	2.199149 $\pm$ 0.00001	8.884098 $\pm$ 0.000009	7.325147 $\pm$ 0.000004	3.9975236 $\pm$ 0.000002
from the Torres et al. (2010) relation					
$M_*$ (M <sub>☉</sub> )	1.12 $\pm$ 0.07	1.37 $\pm$ 0.09	1.37 $\pm$ 0.09	1.10 $\pm$ 0.07	1.23 $\pm$ 0.08
$R_*$ (R <sub>☉</sub> )	0.58 $\pm$ 0.02	1.94 $\pm$ 0.06	1.92 $\pm$ 0.06	1.05 $\pm$ 0.03	1.37 $\pm$ 0.04
from EBLMMASS					
$M_*$ (M <sub>☉</sub> )	0.991 $\pm$ 0.056	1.198 $\pm$ 0.053 1.109 $\pm$ 0.034	1.550 $\pm$ 0.050 1.340 $\pm$ 0.050	1.054 $\pm$ 0.058	1.185 $\pm$ 0.073
$R_*$ (R <sub>☉</sub> )	0.960 $\pm$ 0.016	1.534 $\pm$ 0.041	2.131 $\pm$ 0.088	1.003 $\pm$ 0.0194	1.360 $\pm$ 0.063
$M_2$ (M <sub>☉</sub> )	0.174 $\pm$ 0.006	0.172 $\pm$ 0.004 0.182 $\pm$ 0.005	0.390 $\pm$ 0.009 0.427 $\pm$ 0.009	0.303 $\pm$ 0.014	0.490 $\pm$ 0.018
$R_2$ (R <sub>☉</sub> )	0.288 $\pm$ 0.005	0.189 $\pm$ 0.005 3.98 $\pm$ 0.60	0.361 $\pm$ 0.020 2.35 $\pm$ 0.25	0.287 $\pm$ 0.006	0.408 $\pm$ 0.061
Age (Gyr)	2.34 $\pm$ 2.016	5.81 $\pm$ 1.01	3.80 $\pm$ 0.42	1.10 $\pm$ 1.80	2.300 $\pm$ 0.120
facilities used & number of observations used in the analysis					
SuperWASP [V]	8144	14,369	7872	-	53,259
SAAO 1-m [R, I]	345 [I]	474 [R]	-	-	136 [R]
CTIO [ $g'$ , $r'$ , $i'$ , $z'$ ]	-	-	78 [ $g'$ ] 62 [ $z'$ ] 71 [ $r'$ ] 70 [ $z'$ ]	-	-
Bruce Gary [CBB, $g'$ , $z'$ ]	-	-	-	605 [CBB] 311 [ $g'$ ] 371 [ $z'$ ]	-
CORALIE	20	19	70	-	20
INT	-	-	-	10	-

#### 4.3. EBLM J0218-31

EBLM J0218-31 was observed for three seasons with SuperWASP cameras. **ADD SENTENCE ABOUT ROTATIONAL MODULATION.** We fit 10 photometry measurements with red-

dening to estimate  $T_{\text{eff}} = 6014 \pm 99 \text{ K}$ . The best fitting reddening  $E(B - V) = 0.032 \pm 0.022$  corresponds to a distance approximately **X** parsecs away. J0218-31 is included in the Gaia DR1 catalogue with Source ID 4971670729566470528 and a parallax of 3.98 *pc* (12.98 *ly*). We co-added 53 spectra (SNR  $\sim$  30) to



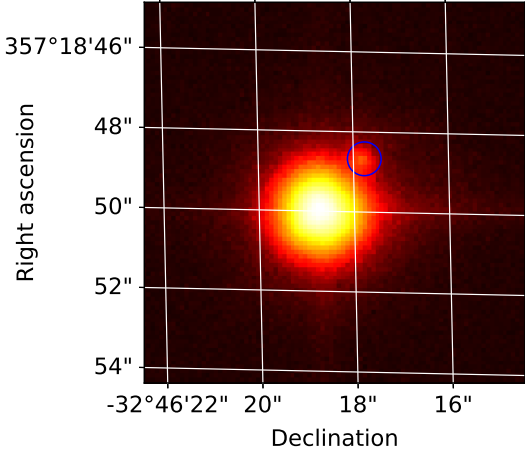


**Fig. 5.** Lucky imaging of J2349-32 revealing a close companion 1.3'' away at a position angle of  $308.6 \pm 0.6$  deg.

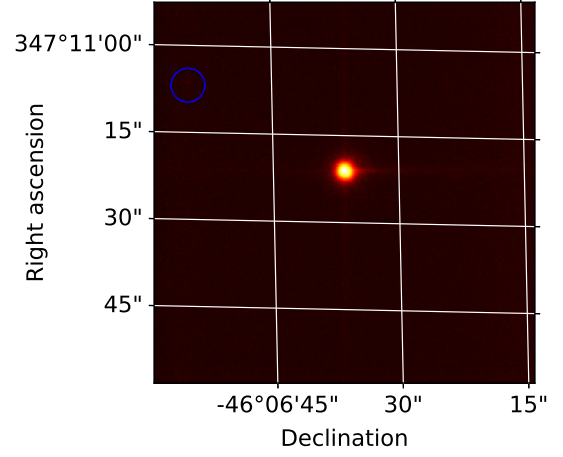


**Fig. 7.** Lucky imaging of J2308-46 revealing a companion 20'' away.

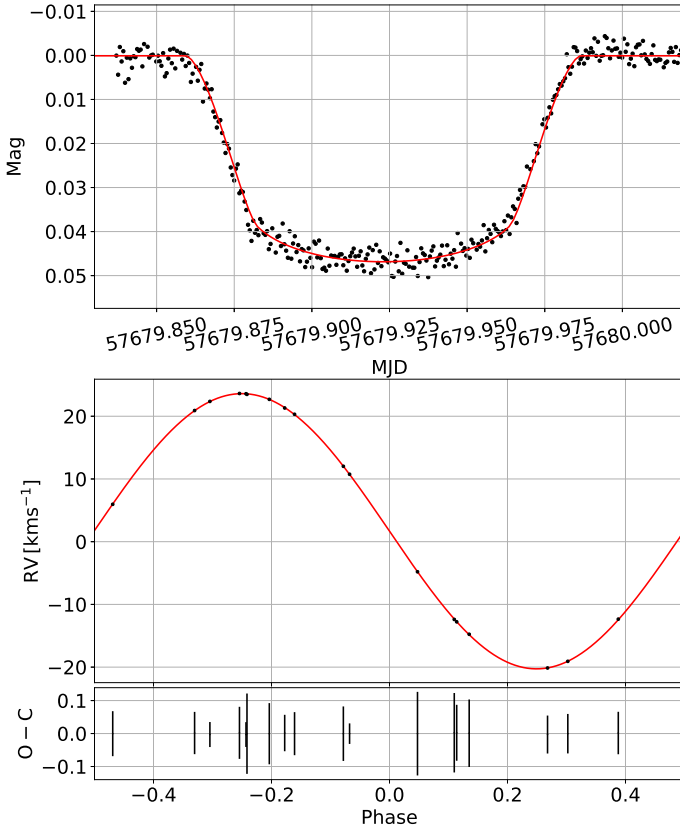


**Fig. 6.** Orbital fit of EBLM J2349-32. (upper panel) The detrended I-band light-curve from the SAAO 1-m telescope is plotted (black) with the best fitting model (red). (middle panel) The phase-folded radial velocity measurements obtained from CORALIE which (drift-corrected; black) with the best model (red). (bottom panel) The residuals between from the best fitting radial velocity model.

estimate  $T_{\text{eff}} = 6099 \pm 86 \text{ K}$  and  $[\text{Fe}/\text{H}] = 0.15 \pm 0.12$  dex. We so find a strong Li detection corresponding to an abundance of  $\log A_{\text{Li}} + 12 \sim 3.24$  suggesting this star has a shallow convective layer unable to burn lithium.

We obtained 28 RM measurements obtained over multiple transits and excluded one as an obvious outlier. We also obtained

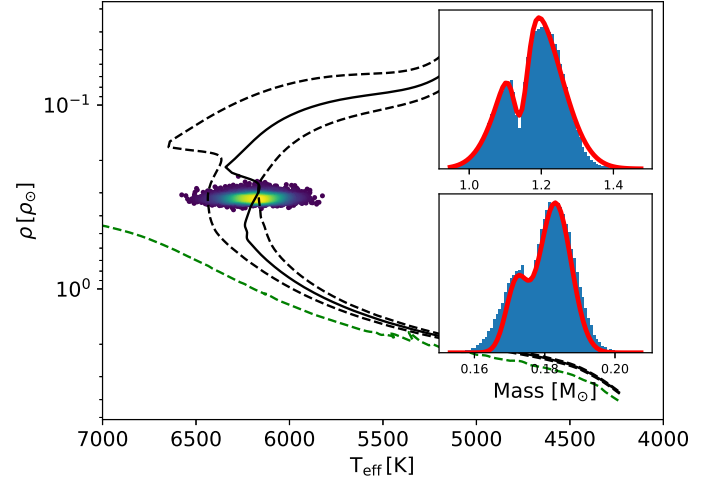


**Fig. 8.** Density- $T_{\text{eff}}$  posterior probability distribution for EBLM J2308-46. Also plotted is the zero-age main sequence at the best fitting  $[\text{Fe}/\text{H}]_i$ , the isochrone for the best fitting age and  $[\text{Fe}/\text{H}]_i$  (solid black) and the isochrones for the best fitting  $[\text{Fe}/\text{H}]_i$  and age, plus and minus the uncertainty of age (dashed-black). We also plot the posterior probability distributions for  $M_*$  and  $M_2$  with double-Gaussian fits to estimate parameter for each model.

70 radial velocity measurements out-of-transit, which indicates a circular system with a Lucy test ( $e \leq 0.03$  to  $6\sigma$ ). We fitted RM and out-of-transit RV measurements with a single follow-up transit in  $g'$ ,  $r'$ ,  $i$  &  $z'$  filters. The best fitting models can be seen in Fig. 11. With the addition of RM measurements, we are able to estimate a spin-orbit mis-alignment of 4 deg and independently determine  $v \sin i$  of  $11.2 \pm 2.2 \text{ km s}^{-1}$  which is in agreement from spectroscopy.

Similar to EBLM J2308-46, J0218-31 has also evolved off the main-sequence and into the Heney hook region (Fig. 10). We fit a double Gaussian model and found that younger ( $2.4 \pm 0.25$  Gyr) solution ( $M_* = 1.55 \pm 0.05 M_{\odot}$ ,  $R_* = 2.13 \pm 0.09 R_{\odot}$ ) is favored with almost twice the probability (24,000 VS 13,500 models) than the older model (Bayes factor of 3.55). We report both solutions in Table. 1 but use the younger solution for the rest of this paper.

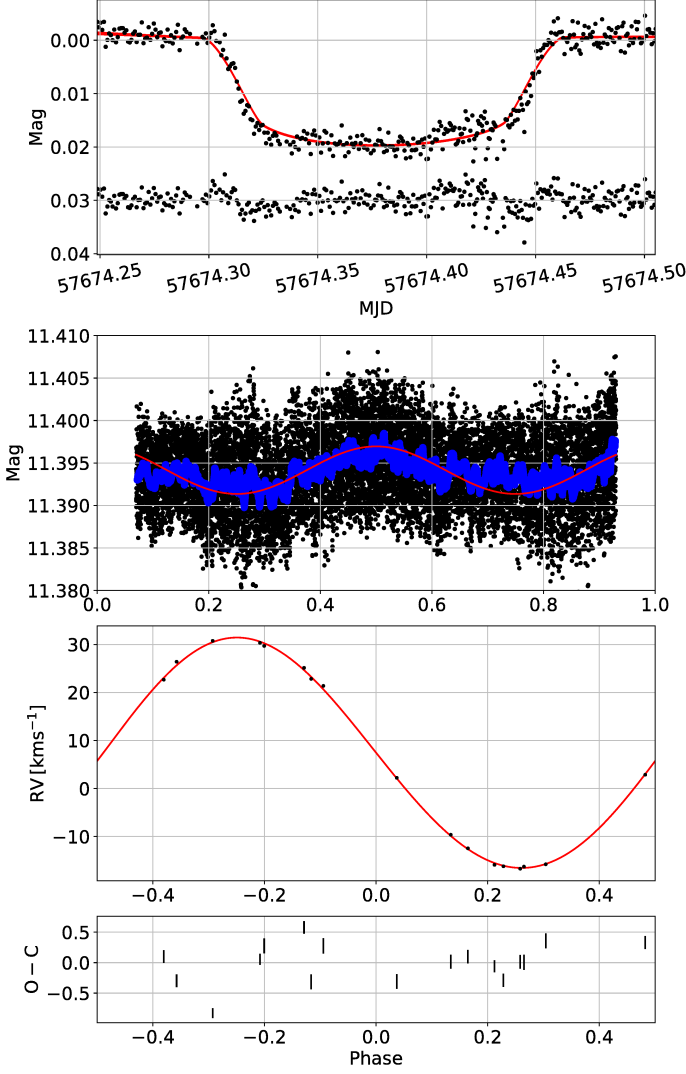


**Fig. 9.** Orbital fit of EBLM J2308-46. (top) R-band transit obtained from the SAAO 1-m telescope (black) with the best fitting model (red). The R-band lightcurve has systematics which could not be detrended with standard techniques, and we include a "hand-crafted" detrending function (blue dashed) in the fitting procedure. (middle top) Phase-folded WASP observations (black) and observations binned into groups of 50 (blue). (middle bottom) Radial velocity measurements from CORALIE (black) with the best fitting model (red). (bottom) Residuals from the best fitting model.

#### 4.4. EBLM J1847+39

EBLM J1847+39 was observed over 4 seasons (2004, 2007, 2009 & 2010) with the SuperWASP. We excluded data from 2004 as only 53 observations were made that year. **ADD SENTENCE ABOUT ROTATIONAL MODULATION.** We fitted 10 photometric data points along with a reddening estimate to determine a  $T_{\text{eff}} = 6205 \pm 218 \text{ K}$ . The best reddening  $E(B - V) = 0.073 \pm 0.042$  corresponds to a distance of  $X \text{ pc}$ . This system was included in the first data release of Gaia (source I.D 2098283457595740288) with a parallax of  $3.67 \text{ pc}$  ( $G\text{-mag} = 11.677$ ). In total, 10 INT spectra were co-added onto a common wavelength base between  $630 - 677 \text{ nm}$  with  $\text{SNR} = 10$ . Because of the relatively short wavelength range, we used the spectral synthesis method on the H-alpha wings to estimate a temperature of  $6200 \pm 400 \text{ K}$  in agreement with photometric fitting. We were able to assess a small number of iron lines in the

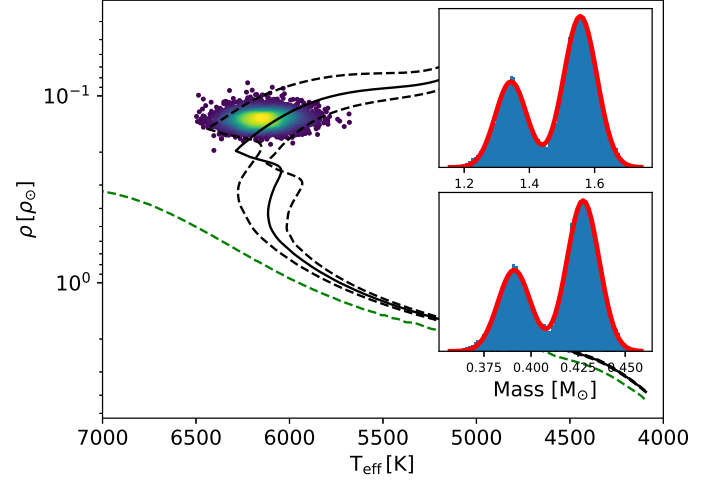


**Fig. 10.** Density- $T_{\text{eff}}$  posterior probability distribution for EBLM J0218-31-46. Also plotted is the zero-age main sequence at the best fitting  $[\text{Fe}/\text{H}]_i$ , the isochrone for the best fitting age and  $[\text{Fe}/\text{H}]_i$  (solid black) and the isochrones for the best fitting  $[\text{Fe}/\text{H}]_i$  and age, plus and minus the uncertainty of age (dashed-black). We also plot the posterior probability distributions for  $M_*$  and  $M_2$  with double-Gaussian fits to estimate parameter for each model.

region around  $\text{H}\alpha$  to estimate  $[\text{Fe}/\text{H}] = -0.25 \pm 0.2 \text{ dex}$ ; there is a larger uncertainty owed to the smaller number of iron lines we were able to fit ( $\approx 5$ ).

A Lucy significance test favors a elliptical solution ( $e = 0.209 \pm 0.014$ ). The RVs were then fitted simultaneously with a single transit in  $\text{CBB}$ ,  $g'$  and  $z'$  filters from HAO to obtain the best orbital solution. We obtained a second independent transit with the CBB filter but excluded it due to poor quality. The best fitting solution from EBLMMASS describes a host star similar to the Sun in mass and size and is the youngest of the entire sample ( $\tau = 1.10 \pm 1.80 \text{ Gyr}$ ). The M-dwarf companion is the second largest of the sample and agrees well with evolutionary models.

#### 4.5. EBLM J1436-13

EBLM J1436-13 was observed over 3 consecutive seasons with SuperWASP cameras. **SENTENCE ABOUT ROTATIONAL MODULATION.** We fit 10 photometry points and an estimate of reddening to determine  $T_{\text{eff}} = 6078 \pm 356 \text{ K}$ . The best fitting reddening  $E(B - V) = 0.031 \pm 0.024$  corresponds to a distance  $X \text{ pc}$  away. This system is included in Gaia DR1 (source I.D 6323183619200685824) but does not include an estimate of parallax. In total, 13 CORALIE spectra we co-added ( $\text{SNR}=30$ ) to estimate  $T_{\text{eff}} = 6312 \pm 86$  and  $[\text{Fe}/\text{H}] = -0.1 \pm 0.12$ , in excellent agreement with sed fitting.

A Lucy significance test found that the circular solution is preferred over an elliptical one. The best fitting orbital solution describes a grazing transit with a moderately high impact parameter ( $b = 0.86 \pm 0.07$ ). We find no significant drifts in period or systematic velocity with time. The best fitting limb-darkening temperature ( $5964 \text{ K}$ ) agrees well with photometric colours and spectroscopy.

The orbital solution with atmospheric parameters combined in EBLMMASS describe the largest M-dwarf companion in the sample ( $M_2 = 0.490 \pm 0.018 M_{\odot}$ ,  $R_2 = 0.408 \pm 0.061 R_{\odot}$ ). The grazing orbital geometry increases the uncertainty of  $R_*$  and  $R_2$  which is at odds with the aim of the EBLM project.

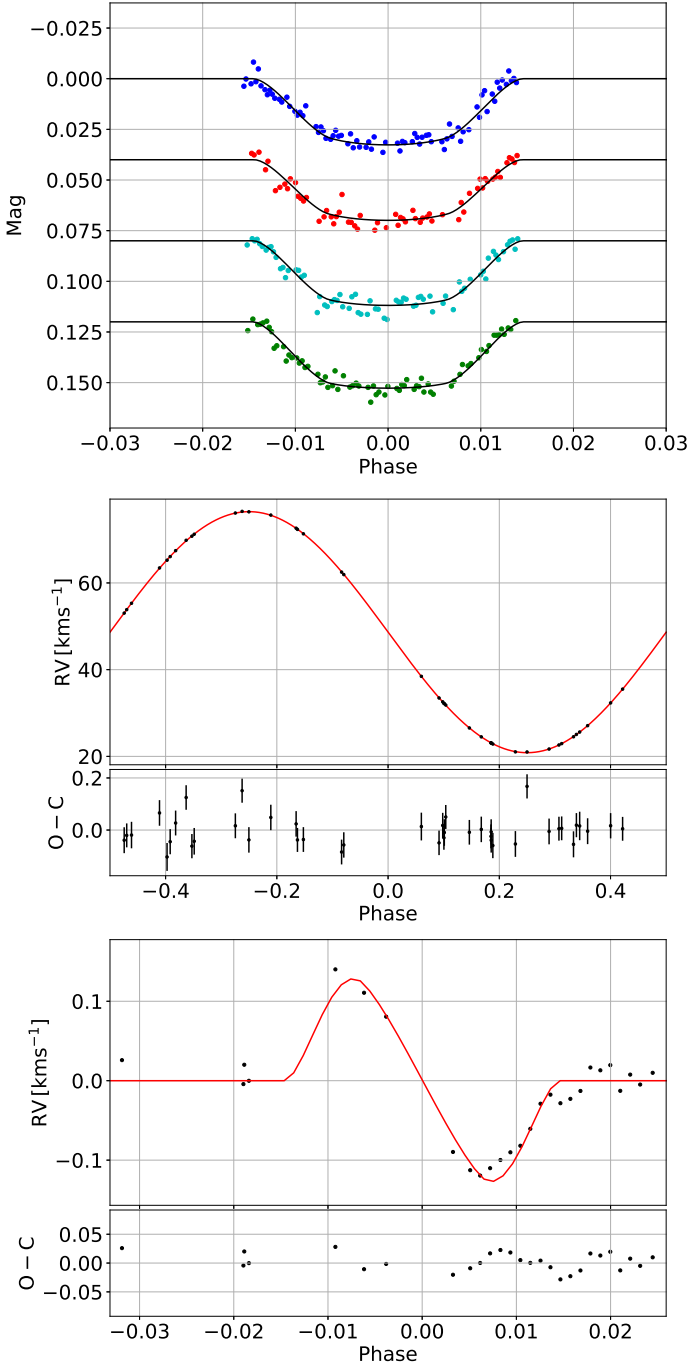


**Fig. 11.** Orbital fit for EBLM J0218-31. (top panel) Transit photometry from CTIO in  $g'$  (blue),  $r'$  (red),  $i'$  (cyan) and  $z'$  (green) with best fitting models shown in black. (middle panel) Radial velocity measurements from CORALIE with best fitting models plotted in red, along with residuals from the model. (bottom panel) Radial velocity measurements during transit (the Rossiter–McLaughlin effect; black) with the best fitting model (red).

## 5. Tertiary components

We fitted a drift term ( $dV_0/dt$ ) to assess drifts in systematic velocity which may indicate a third body. This is most likely a tertiary star but possibly a circumbinary brown dwarf or massive planet. A study of 118 EBLM systems by (Triaud et al. 2017) yielded a tertiary rate of 17.8 % (21). This fraction is suggested to increase with decreasing orbital period (Tokovinin et al. 2006)

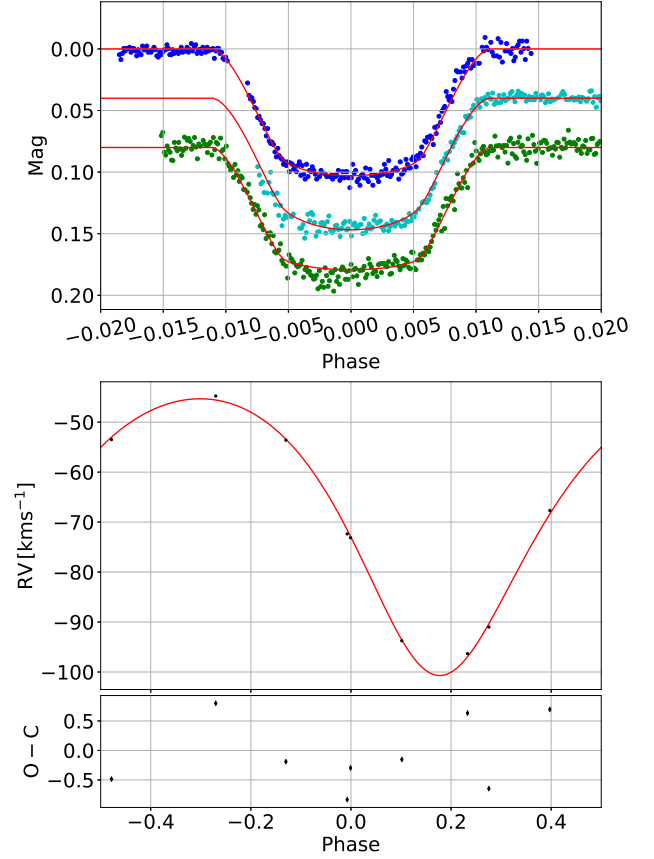


**Fig. 12.** Orbital fit of EBLM J1847+39. (top panel) Single transits from the HAO in filters CBB (blue),  $g'$  (cyan) and  $z'$  (green) with best fitting models (red). (bottom panel) Radial velocity measurements are phase folded and corrected for drifts in systematic velocity (black) with the best fitting model (red) and residual of the models.

but is not seen for the 21 EBLM systems presented by Triaud et al. (2017). We find that 2 systems (EBLM J2308-46 & J0218-31) have orbital solutions which tend to non-zero values of  $dV_0/dt$ . For J2308-46 we find the best fitting drift in systematic velocity is non-zero to  $2\sigma$  ( $-0.0004[2] \text{ kms}^{-2}$ )

## 6. Systematic effects on determining mass, radius and age

With the success of Kepler (Borucki et al. 2010), K2 (Howell et al. 2014) and future space missions we will soon be able to measure mass and radius of star to 0.1 % precision. These measurements will provide excellent tests for evolutionary models and increase reliability of empirical calibrations. For EBLMs, we choose to use well-understood evolutionary models of the solar-like host star to determine mass with the precision of a few percent. We use fixed values of  $\alpha_{MLT}$  (1.4) and He enhancement (0.0) which have a large uncertainty that cannot be ignored for solar models. Fitting transit photometry also depends on assumptions of null contamination in the aperture and limb-darkening profiles. These are all ignored assumptions which could introduce additional uncertainty. In the following sections we explore a few of these, and the impact they may have on our measurements.

**Table 2.** The difference in mass and radius of the primary star ( $\star$ ) and the secondary (2; measured values subtracted from those in Tab. 1) determined for various scenarios. We re-measure the mass and radius of all the EBLM light-curves with % 10 % third light ( $l_3$ ). We also re-fit light-curves using a quadratic limb-darkening law over a Claret law ( $ldy$ ). We also re-measure mass and radius using the same orbital solutions from Sect. 4 and changing the mixing length parameter from 1.50 to 1.78 ( $\alpha_{mlt}$ ) and a change in helium enhancement values from 0.00 to 0.02 ( $Y$ ).

	$\Delta R_{\star, l_3}$	$\Delta R_{2, l_3}$	$\Delta R_{\star, ldy}$	$\Delta R_{2, ldy}$	$\Delta M_{\star, \alpha_{mlt}}$	$\Delta M_{2, \alpha_{mlt}}$	$\Delta Age_{\alpha_{mlt}}$	$\Delta M_{\star, Y}$	$\Delta M_{2, Y}$	$\Delta Age_Y$
J2349-32	-0.002	-0.016	-0.014	-0.002	-0.037	-0.004	2.208	0.048	0.005	-0.853
J2308-46	-0.003	-0.011	-0.017	-0.001	-0.045	-0.003	1.703	0.056	0.004	-1.201
J0218-31	-0.007	-0.012	-0.005	-0.002	-0.057	-0.001	0.503	0.041	0.006	-0.254
J1847+39	-0.008	-0.016	-0.015	-0.004	-0.046	-0.001	1.071	0.052	0.009	-0.82
J1436-13*	-0.162	-0.064	-0.059	-0.090	-0.024	-0.005	-0.135	0.043	0.011	-1.15
$\bar{x}$	-0.005	-0.013	-0.012	-0.003	-0.046	-0.002	1.070	0.050	0.007	0.855

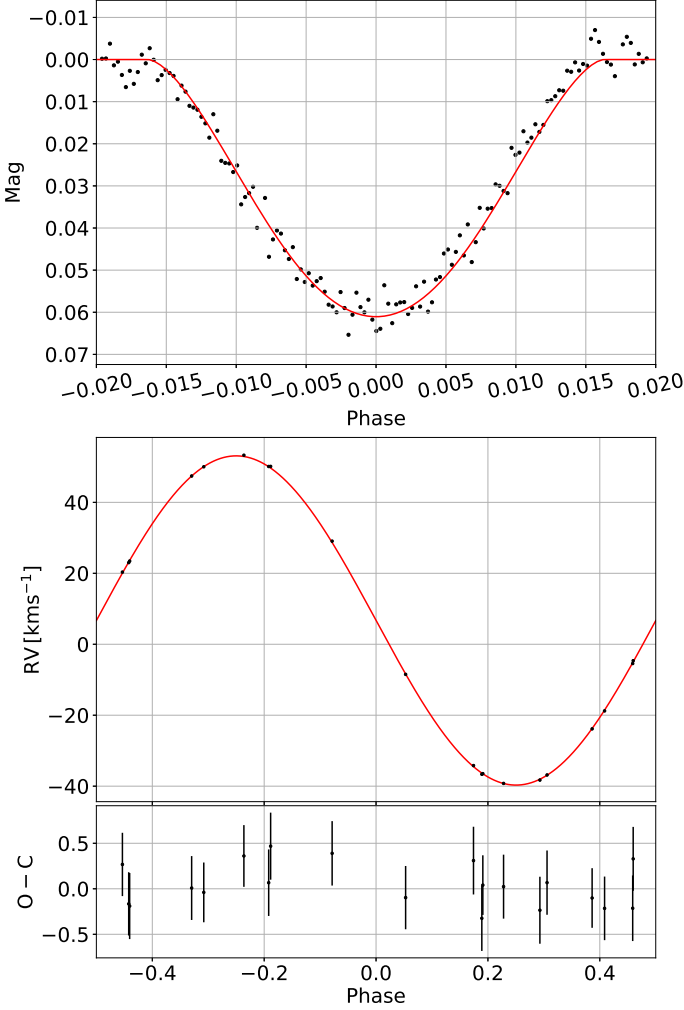


**Fig. 13.** Orbital fit of EBLM J1436-13. (top panel) A single transit obtained from SAAO in R filter (black) and the best fitting transit model (red). (bottom panel) Radial velocity measurements from CORALIE (black) with best fitting model (red) and residuals.

### 6.1. Evolution ambiguity, $\alpha_{MLT}$ and $Y_{He}$

The grids used in EBLMMASS have a set value of helium enhancement,  $Y = 0$ , and mixing length parameter,  $\alpha_{MLT} = 1.78$  which have been calibrated on the Sun. As noted by Maxted et al. (2015a), this is subject to some level of uncertainty and was addressed by (Maxted et al. 2015b). They estimate the uncertainty of  $M_{\star}$  and age for 28 transiting stars by assuming an er-

ror of 0.2 for  $\alpha_{MLT}$  and 0.02 for initial helium enhancement,  $Y$  for each star (denoted as  $\sigma_{M_{\star}, \alpha}$ ,  $\sigma_{\star, Y}$ ,  $\sigma_{\tau, \alpha}$  and  $\sigma_{\tau, Y}$ ). They find mass and  $\tau$  uncertainties from  $Y$  and  $\alpha_{mlt}$  can rival internal errors from EBLMMASS. We note that the sample used in Maxted et al. (2015b) consists primarily of stars less massive than the Sun, while our stars are generally larger. Three grids come with EBLMMASS; 1.  $\alpha_{MLT} = 1.78$ ,  $Y = 0.00$ , 2.  $\alpha_{MLT} = 1.5$ ,  $Y = 0.00$  and 3.  $\alpha_{MLT} = 1.78$ ,  $Y = 0.02$ ; we used grid 1 in Table. 4. We re-measured the mass, radius and  $\tau$  of both components with the grids 2 and 3 to assess the impact of  $\alpha_{mlt}$  and  $Y$ . We use the same orbital solution for each of the 5 EBLM systems and use grid 2 to assess the impact of  $\Delta\alpha_{MLT} = 0.28$  and grid 3 to assess the impact of  $\Delta Y = 0.02$ .

The mass uncertainties in Table. 2 corresponding to  $\Delta\alpha_{mlt} = 0.28$  are on the order of 2 – 3% and is similar to those found by Maxted et al. (2015b). Helium enhancement typically introduces a larger mass uncertainties around 4 – 5%. The opposite is seen for  $\tau$  determinations, where  $\Delta\alpha_{MLT} = 0.28$  introduces an uncertainty by 1.07 Gyr and  $\Delta Y = 0.02$  introduces an uncertainty of  $\Delta\tau = 0.86$  Gyr. The typical uncertainty in  $\tau$  from EBLMMASS for these EBLM systems is around 1 Gyr and can produce significant systematic offsets. The quadratic combination of uncertainty for  $M_2$  introduced by  $\alpha_{mlt}$  and  $Y$  is around  $0.01 M_{\odot}$  (2 – 4 % for a  $0.4 M_{\odot}$  M-dwarf).

A further limitation arises when the primary star has evolved into post-main sequence blue hook (Heney hook). Two host-stars in our sample (J2308-46 and J0218-31) are in this region leading to dual solutions for  $M_{\star}$  and  $\tau$ . A single solution is preferred for both these systems but there will always be some ambiguity until further mass constraints can be obtained. Until then, these systems should not contribute to empirical calibrations. One approach for the EBLM project could be to pre-select cooler host stars ( $\leq 6100$  K) to rule out approaching the Heney hook. A solution may lay in the increased contrast between a FGK star and an M-dwarf in the infrared. It could be possible to detect molecular lines (VO, TiO, CaH, e.t.c) associated with an M-dwarf from a infrared spectra enabling radial velocity measurements of the secondary component turning an SB1 into an SB2 and allow us to break the degeneracy around the Heney hook.

### 6.2. Third light effect

The analysis of 118 EBLM systems by (Triaud et al. 2017) found a tertiary rate of 17.8 %. These are most likely to be companion stars which could effect the orbital solution. Lacking imaging provides constraints on nearby contaminating objects. For EBLMs J2349-32 and J2308-46, we find that close companions resolved by lucky imaging do not significantly contaminate

follow-up photometry. For EBLMs J0218-31 and J1847+39 we have transit photometry in different pass bands with similar measured transit depths ( $k$ ) to  $1\sigma$ . For EBLM J1436-13 we must rely on existing surveys to identify nearby stars which may contaminate follow-up photometry. By inspection of the GAIA survey DR1 (resolution of  $\sim 4''$ ) we find no evidence of blends or contamination. Lucky imaging typically has a resolution of  $0.1''$  corresponding to an orbital separation of  $\sim 110$  AU at the average distance of these five targets ( $\sim 200$  pc). The latest installment of the EBLM project (Triaud et al. 2017) predicts a tertiary rate of  $21/118 = 17.8\%$  from drifts in the systematic radial velocity; these tertiary components have periods of decades corresponding to a semi-major axis below 110 AU and would be difficult/impossible to resolve through lucky imaging. The low signal-to-noise spectra from CORALIE eliminates unresolved blends above 30 % contamination by inspection of cross-correlation functions, but we do not have capabilities to identify unresolved companions contributing 10-20 % of the light.

Including third light as a free parameter in the orbital fit changes the shape and depth of a light-curve leading to degeneracies between  $R_*$ ,  $k$  and  $b$ . We assess this by re-fitting the orbital solution for all stars assuming a worst case scenario of 10 % light contamination. From this fit, we combine best fitting values of  $R_*/a$ ,  $b$ , and  $k$  and their uncertainties with nominal values from the original fit to re-determine  $R_*$  and  $R_2$  from EBLMMASS (first two columns in Table. 2). On average, we find a 3-5% increase in  $R_2$  when third light is fixed to 10 %; we ignore EBLM J1436-13 from this discourse due to the grazing nature of transit. A worst case scenario resulting in an increase of  $R_2$  by 5 % could account for inflated radii noted in the literature (typically 3 – 5 %; (Spada et al. 2013)).

### 6.3. Limb darkening

Limb darkening is a second order effect crucial for determining  $R_*$ ,  $K$  and  $b$ . For this work, we use the Claret 4-parameter law (Claret 2000),

$$\frac{I_u}{I_0} = 1 - \sum_{i=1}^4 a_i (1 - \mu^{\frac{1}{2}i}), \quad (8)$$

where  $\mu = \cos \gamma$  and  $\gamma$  is the angle between a line normal to the stellar surface and the line of sight of the observer. The coefficient tables we use are provided by Claret and Bloemen (Claret & Bloemen 2011) for Kepler, Stromgren, Johnson-Cousins and Sloan pass-bands for ATLAS stellar atmosphere models assuming a micro-turbulent velocity  $\xi = 2 \text{ km s}^{-1}$ . For the SDSS pass-bands ( $u'$ ,  $g'$ ,  $r'$ ,  $i'$ ,  $z'$ ) we use tables from Claret (2004). We interpolate these tables for a given  $T_{\text{eff}}$ ,  $[\text{Fe}/\text{H}]$  and  $\log g$  to obtain 4 limb darkening parameters and a gravity darkening coefficient (through ELLC). As described in Sect. 3.4, we allow the limb-darkening temperature,  $T_{\text{eff}}$ , to vary as a free parameter with a Gaussian prior from spectroscopy, and fix  $\log g$  and  $[\text{Fe}/\text{H}]$  to values from wavelet analysis. Other studies use a quadratic limb-darkening law (Kopal 1950) with only 2 parameters,

$$\frac{I_u}{I_0} = 1 - \sum_{i=1}^2 a_i (1 - \mu)^i, \quad (9)$$

and allow both coefficients to vary in the fit using the de-correlated parameters  $a_+ = a_1 + a_2$  and  $a_- = a_1 - a_2$  (Brown et al.

2001). Alternate de-correlation parameters have been suggested by Kipping (2013):  $q_1 = (a_1 + a_2)^2$  and  $q_2 = 0.5 \times a_1(a_1 + a_2)^{-1}$ .

We assess the choice of limb-darkening law on  $R_*$  and  $R_2$  by re-fitting using each system using a quadratic limb darkening law (Eq. 9) instead of the Claret 4 parameter law. We generate coefficients  $a_1$  &  $a_2$  for each pass-band for each filter using the python package LDTK (see Table. X; Parviainen & Aigrain 2015). LDTK uses uncertainties from  $T_{\text{eff}}$ ,  $[\text{Fe}/\text{H}]$  and  $\log g$  to estimate uncertainties in the calculated values of  $a_1$  and  $a_2$  ( $\sigma_{a_1}$  and  $\sigma_{a_2}$ ). We use these uncertainties to apply Gaussian priors to  $a_1$  and  $a_2$  to stop the sampler tending to unrealistic values. The best fitting values of  $R_*/a$ ,  $k$ , and  $b$  and their uncertainties are combined with values from the normal orbital solution in Sect. 4 so that the light-curve information changes. These are then used in EBLMMASS to re-determine the radius  $R_*$  and  $R_2$ .

In Table. 2 we find that the uncertainty introduced by choice of limb-darkening law is less than introduced by third light. The majority of stars see a reduction in  $R_*$  and  $R_2$  below 1 %. A study by Csizmadia et al. (2013) for exoplanets concludes that fixing the limb-darkening coefficients to theoretical values does not allow the determination of  $R_2$  to better than 1 – 10%; a reason why we fitted  $a_1$  &  $a_2$ . Intertwined in this is stellar activity, spots and faculae, should any star be active. This is a time-dependent effect which varies at each transit event and can modify the limb-darkening values far from what is predicted. One conclusion from Csizmadia et al. (2013) is that a star with 0.5 % spot coverage can still introduce a 1% uncertainty on  $k$ ; a result akin to Table.2.

## 7. Conclusion

Spectroscopic orbits for 5 EBLM systems were obtained as part of the EBLM project and provide constraints on the masses of both components in the system. For J0218-31 we have radial velocity measurements covering the Rossiter McLaughlin effect providing information about the obliquity of the system. The atmospheric parameters of the primary star were determined from these spectra using wavelet analysis and spectral fitting. To determine the radii of both components we required follow-up photometry as SuperWASP photometry is not sufficient to determine radius to a precision of a few percent. The best fitting orbital solution was combined with atmospheric parameters (in EBLMMASS) to determine the mass and radius of each system.

For EBLM J2349-32 we have good estimates of mass and radii for both components. For J1847+39 we only have INT spectra covering the  $\text{H}\alpha$  region leading to a relatively larger uncertainty of  $[\text{Fe}/\text{H}]$ , mass and age of components in the system. For EBLM J0218-31 and J2308-46 we find that the host star has evolved into the post main-sequence blue hook resulting in two solutions for  $M_*$ ,  $M_2$ , &  $\tau$ . For each of these systems there is a favored solution but ambiguity will remain until further constraints on mass and radii can be obtained. The final system, EBLM J1436-13, is a grazing transit resulting in an increase in uncertainty for the radius of the system.

We investigated the deviation in radii determined when using a quadratic limb darkening law over the Claret law which resulted in a 1% reduction for  $R_*$  and  $R_2$ . We also assess the effect of  $\alpha_{\text{mlt}}$  and helium enhancement ( $Y$ ) in evolutionary models on the masses and ages of the system. We find that increasing  $Y$  by 0.02 increases the determined masses of the primary and secondary by 4–5 % and decreases the age of the system by 0.8 Gyr. Increasing the mixing length parameter by 0.28 decreases the age by half as much relative to changing  $Y$ , but find a larger scatter age ( $\sim 1.07$  Gyr). These uncertainties may seem insignificant



relative to the internal precision of EBLMMASS but are enough to introduce systematics for mass and radii measurements which could lower the reliability of empirical calibrations.

## References

- Baraffe, I., Chabrier, G., Barman, T. S., Allard, F., & Hauschildt, P. H. 2003, *A&A*, 402, 701
- Baranne, A., Queloz, D., Mayor, M., et al. 1996, *A&AS*, 119, 373
- Beatty, T. G., Fernández, J. M., Latham, D. W., et al. 2007, *ApJ*, 663, 573
- Bessell, M. S. 2000, *PASP*, 112, 961
- Bessell, M. S. 2005, *ARA&A*, 43, 293
- Blanco-Cuaresma, S., Anderson, R. I., Eyer, L., & Mowlavi, N. 2017, in *Highlights on Spanish Astrophysics IX*, ed. S. Arribas, A. Alonso-Herrero, F. Figueras, C. Hernández-Monteagudo, A. Sánchez-Lavega, & S. Pérez-Hoyos, 495–495
- Borucki, W. J., Koch, D., Basri, G., et al. 2010, *Science*, 327, 977
- Boyajian, T. S., von Braun, K., van Belle, G., et al. 2013, *ApJ*, 771, 40
- Brown, T. M., Charbonneau, D., Gilliland, R. L., Noyes, R. W., & Burrows, A. 2001, *ApJ*, 552, 699
- Casagrande, L., Flynn, C., & Bessell, M. 2008, *MNRAS*, 389, 585
- Chabrier, G., Gallardo, J., & Baraffe, I. 2007, *A&A*, 472, L17
- Claret, A. 2000, *A&A*, 363, 1081
- Claret, A. 2004, *A&A*, 428, 1001
- Claret, A. & Bloemen, S. 2011, *A&A*, 529, A75
- Csizmadia, S., Pasternacki, T., Dreyer, C., et al. 2013, *A&A*, 549, A9
- Davenport, J. R. A., Ivezić, Z., Becker, A. C., et al. 2014, *MNRAS*, 440, 3430
- Epchtein, N., de Batz, B., Capolani, L., et al. 1997, *The Messenger*, 87, 27
- Evans, D. F., Southworth, J., Maxted, P. F. L., et al. 2016, *A&A*, 589, A58
- Fiorucci, M. & Munari, U. 2003, *A&A*, 401, 781
- Foreman-Mackey, D., Agol, E., Angus, R., & Ambikasaran, S. 2017, *ArXiv*
- Foreman-Mackey, D., Hogg, D. W., Lang, D., & Goodman, J. 2013, *PASP*, 125, 306
- Fortier, A., Beck, T., Benz, W., et al. 2014, in *Proc. SPIE, Vol. 9143, Space Telescopes and Instrumentation 2014: Optical, Infrared, and Millimeter Wave*, 91432J
- Gaia Collaboration, Brown, A. G. A., Vallenari, A., et al. 2016a, *A&A*, 595, A2
- Gaia Collaboration, Prusti, T., de Bruijne, J. H. J., et al. 2016b, *A&A*, 595, A1
- Gaidos, E., Mann, A. W., Lépine, S., et al. 2014, *MNRAS*, 443, 2561
- Gómez Maqueo Chew, Y., Morales, J. C., Faedi, F., et al. 2014, *A&A*, 572, A50
- Griffin, R. F., Mayor, M., Pont, F., & Udry, S. 1997, *The Observatory*, 117, 288
- Harpsøe, K. B. W., Jørgensen, U. G., Andersen, M. I., & Grundahl, F. 2012, *A&A*, 542, A23
- Hebb, L., Collier-Cameron, A., Loeillet, B., et al. 2009, *ApJ*, 693, 1920
- Henden, A. A., Templeton, M., Terrell, D., et al. 2016, *VizieR Online Data Catalog*, 2336
- Hilditch, R. W. 2001, *An Introduction to Close Binary Stars*, 392
- Høg, E., Fabricius, C., Makarov, V. V., et al. 2000, *A&A*, 355, L27
- Howell, S. B., Sobek, C., Haas, M., et al. 2014, *PASP*, 126, 398
- Kipping, D. M. 2013, *MNRAS*, 435, 2152
- Kopal, Z. 1950, *Harvard College Observatory Circular*, 454, 1
- Kraft, R. P. 1967, *ApJ*, 150, 551
- Lenz, P. & Breger, M. 2005, *Communications in Asteroseismology*, 146, 53
- Levrard, B., Winisdoerffer, C., & Chabrier, G. 2009, *ApJ*, 692, L9
- Lucy, L. B. 2013, *A&A*, 551, A47
- Mamajek, E. E., Prsa, A., Torres, G., et al. 2015, *ArXiv e-prints* [arXiv:1510.07674]
- Mann, A. W., Feiden, G. A., Gaidos, E., Boyajian, T., & von Braun, K. 2015, *ApJ*, 804, 64
- Matsumura, S., Peale, S. J., & Rasio, F. A. 2010, *ApJ*, 725, 1995
- Maxted, P. F. L. 2016, *A&A*, 591, A111
- Maxted, P. F. L., Bloemen, S., Heber, U., et al. 2014, *MNRAS*, 437, 1681
- Maxted, P. F. L., Serenelli, A. M., & Southworth, J. 2015a, *A&A*, 575, A36
- Maxted, P. F. L., Serenelli, A. M., & Southworth, J. 2015b, *A&A*, 577, A90
- Nefs, S. V., Birkby, J. L., Snellen, I. A. G., et al. 2013, *MNRAS*, 431, 3240
- Ofir, A., Gandolfi, D., Buchhave, L., et al. 2012, *MNRAS*, 423, L1
- Parviainen, H. & Aigrain, S. 2015, *MNRAS*, 453, 3821
- Pollacco, D. L., Skillen, I., Collier Cameron, A., et al. 2006, *PASP*, 118, 1407
- Queloz, D., Mayor, M., Udry, S., et al. 2001, *The Messenger*, 105, 1
- Ricker, G. R., Winn, J. N., Vanderspek, R., et al. 2014, in *Proc. SPIE, Vol. 9143, Space Telescopes and Instrumentation 2014: Optical, Infrared, and Millimeter Wave*, 914320
- Rojas-Ayala, B., Covey, K. R., Muirhead, P. S., & Lloyd, J. P. 2012, *ApJ*, 748, 93
- Schlafly, E. F. & Finkbeiner, D. P. 2011, *ApJ*, 737, 103
- Skottfelt, J., Bramich, D. M., Hundertmark, M., et al. 2015, *A&A*, 574, A54
- Skrutskie, M. F., Cutri, R. M., Stiening, R., et al. 2006, *AJ*, 131, 1163
- Smith, A. M. S. & WASP Consortium. 2014, *Contributions of the Astronomical Observatory Skalnaté Pleso*, 43, 500
- Southworth, J. 2011, *MNRAS*, 417, 2166
- Southworth, J., Hinse, T. C., Jørgensen, U. G., et al. 2009, *MNRAS*, 396, 1023
- Spada, F., Demarque, P., Kim, Y.-C., & Sills, A. 2013, *ApJ*, 776, 87
- Tokovinin, A., Thomas, S., Sterzik, M., & Udry, S. 2006, *A&A*, 450, 681
- Torres, G. 2013, *Astronomische Nachrichten*, 334, 4
- Triaud, A. H. M. J., Anderson, D. R., Collier Cameron, A., et al. 2013a, *A&A*, 551, A80
- Triaud, A. H. M. J., Collier Cameron, A., Queloz, D., et al. 2010, *A&A*, 524, A25
- Triaud, A. H. M. J., Hebb, L., Anderson, D. R., et al. 2013b, *A&A*, 549, A18
- Triaud, A. H. M. J., Martin, D. V., Ségransan, D., et al. 2017, *ArXiv e-prints* [arXiv:1707.07521]
- von Boetticher, A., Triaud, A. H. M. J., Queloz, D., et al. 2017, *ArXiv e-prints* [arXiv:1706.08781]
- Weiss, A. & Schlattl, H. 2008, *Ap&SS*, 316, 99
- Wilson, D. M., Gillon, M., Hellier, C., et al. 2008, *ApJ*, 675, L113
- Zhou, G., Bayliss, D., Hartman, J. D., et al. 2014, *MNRAS*, 437, 2831

## 8. Acknowledgements

This work has made use of data from the European Space Agency (ESA) mission *Gaia* (<https://www.cosmos.esa.int/gaia>), processed by the *Gaia* Data Processing and Analysis Consortium (DPAC, <https://www.cosmos.esa.int/web/gaia/dpac/consortium>). Funding for the DPAC has been provided by national institutions, in particular the institutions participating in the *Gaia* Multilateral Agreement.